

6

Instabilities of Shallow-Water Flows with Vertical Shear in the Rotating Annulus

Jonathan Gula¹ and Vladimir Zeitlin²

6.1. INTRODUCTION

There is a long tradition of experiments in differentially rotating annuli in order to understand the baroclinic instability and, more generally, the instabilities of fronts in geophysical fluid dynamics (GFD) [Hide, 1958; Fultz *et al.*, 1959; Hide and Fowles, 1965; Hart, 1972]. Recently the interest in such experiments was revived in the context of the so-called spontaneous emission of inertia-gravity waves by balanced flows (see Ford [1994], O'Sullivan and Dunkerton [1995], and the references in the special collection of *Journal of Atmospheric Sciences* on this subject, Dunkerton *et al.* [2008]). Thus, short-wave patterns coupled to the baroclinic Rossby waves were observed in independent experiments [Lovegrove *et al.*, 2000; Williams *et al.*, 2005; Flór, 2007; Flór *et al.*, 2011] on instabilities of the two-layer rotating flows in the annulus at high enough Rossby numbers.

On the other hand, the classical experiments on unstable density (coastal) currents by Griffiths and Linden [1982] also used annular geometry and a two-layer setting, with lighter fluid overflowing the denser one in the rotating tank. Recently, similar experiments, but with sloping bottom, were performed by Pennel *et al.* [2012].

Motivated by all these experiments, we undertook a thorough stability analysis of a two-layer shallow-water system in the rotating annulus both with the rigid lid and with a free surface and outcropping interface. Our main goal in the rigid-lid configuration was to check to what extent the ageostrophic short-wave instabilities in

shallow water may account for experimental observations. In the outcropping configuration it was instructive to see to what extent the simple two-layer shallow water-theory reproduces the experiment.

The experiments mentioned above are not strictly speaking shallow-water ones, although no pronounced vertical structure was observed, as to our knowledge. The results we present below may serve, nevertheless, to understand the vertically averaged behavior of the full system. Moreover, Williams *et al.* [2005] interpreted their experiments in terms of shallow-water dynamics, referring to Ford [1994]. As to the density currents, their instabilities are traditionally studied with shallow-water models, as in the classical paper by Griffiths *et al.* [1982]. Being standard in GFD, the two-layer shallow-water approximation is a reasonable compromise between the realistic representation of the observed fluid flow and the computational effort (and amount of resources) necessary for a full stability analysis. It is, in addition, self-consistent and universal, as, for example, the fine vertical structure of the flow may vary from one experiment to another.

In Section 6.2 we present our results for the superrotating rigid-lid configurations (following Gula *et al.* [2009b], where most of them were published). In Section 6.3 we give new results for the free surface configuration with outcropping, and in Section 6.4 we analyze the influence of bathymetry on the instabilities.

6.2. STABILITY OF FRONTS UNDER RIGID LID

A typical configuration used in laboratory experiments by Williams *et al.* [2005] and Flór *et al.* [2011] is presented in Figure 6.1. The annulus has an inner vertical sidewall of radius r_1 , an outer vertical sidewall of radius r_2 , and a

¹Institute for Geophysics and Planetary Physics, University of California, Los Angeles, California, United States of America.

²Laboratoire de Météorologie Dynamique, École Normale Supérieure; and Université Pierre et Marie Curie, Paris, France.

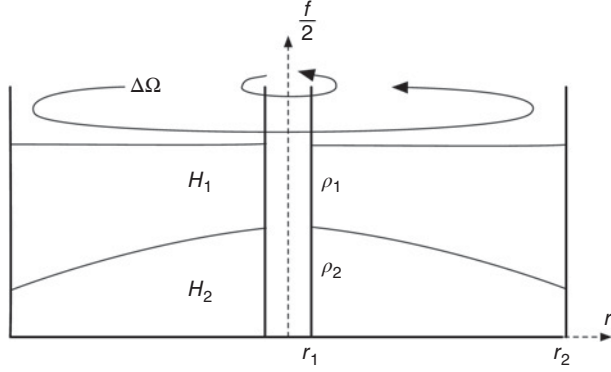


Figure 6.1. Schematic representation of a two-layer flow in the annulus with a superrotating lid.

total depth $2H_0$. The radial width of the annulus is therefore $r_2 - r_1$, and the two layers have equal depths H_0 at rest. The base and the lid are both horizontal and flat. The angular velocity about the axis of symmetry is Ω , and the upper lid is superrotating at $\Omega + \Delta\Omega$. This differential rotation provides a vertical velocity shear of the balanced basic state that is close to solid-body rotation of each fluid layer with different angular velocities. Such a state will be represented in the stability analysis that follows by a cyclogeostrophic equilibrium in each layer, with linear radial profile of the azimuthal velocity, within the rotating two-layer shallow-water model. In order to fulfil a complete linear stability analysis, we use below the collocation method.

Our analysis is purely inviscid; however, in the experiment the mean axisymmetric flow is controlled by friction. As is well known [see, e.g., Hart, 1972], Ekman, Stewartson, and shear boundary layers are present in the two-layer rotating fluid in the tank, and the related torques are acting upon the quasi-inviscid interior. Moreover, the interfacial layer has an internal structure depending on whether two fluids are immiscible or not (see Chapter 11). All this internal structure will be neglected in what follows, and the layers will be considered to be in solid rotation.

6.2.1. Equations of Motion, Basic States, and Linear Stability Problem

Consider the two-layer rotating shallow-water model on the plane rotating with constant angular velocity Ω . The momentum and continuity equations are written in polar coordinates as

$$\begin{aligned} D_j u_j - \left(f + \frac{v_j}{r}\right) v_j - r\Omega^2 &= -\partial_r \Pi_j, \\ D_j v_j + \left(f + \frac{v_j}{r}\right) u_j &= -\frac{\partial_\theta \Pi_j}{r}, \\ D_j h_j + h_j \nabla \cdot \mathbf{v}_j &= 0, \end{aligned} \quad (6.1)$$

where $\mathbf{v}_j = (u_j, v_j)$, h_j , and Π_j are velocity (radial, azimuthal), thickness, and pressure normalized by density (geopotential), respectively, in the j th layer (counted from the top), $j = 1, 2$; f is the Coriolis parameter, $f = 2\Omega$; and D_j denote Lagrangian derivatives in respective layers. The boundary conditions are $u = 0$ at $r = r_1, r_2$.

By introducing the time scale $1/f$, the horizontal scale $r_0 = r_2 - r_1$, the vertical scale H_0 , and the velocity scale $V_0 = fr_0$, we use nondimensional variables from now on without changing notation. By linearizing about a steady state with constant azimuthal velocities $V_1 \neq V_2$, we obtain the following nondimensional equations (the ageostrophic version of the Phillips model in cylindrical geometry):

$$\begin{aligned} \partial_t u_j + \frac{V_j}{r} \partial_\theta u_j - v_j - 2 \frac{V_j v_j}{r} &= -\partial_r \pi_j, \\ \partial_t v_j + u_j \partial_r V_j + \frac{V_j}{r} \partial_\theta v_j + u_j + \frac{V_j u_j}{r} &= -\frac{\partial_\theta \pi_j}{r}, \\ \partial_t h_j + \frac{1}{r} (r H_j u_j)_r + \frac{1}{r} H_j \partial_\theta v_j + \frac{V_j}{r} \partial_\theta h_j &= 0, \end{aligned} \quad (6.2)$$

where the pressure perturbations in the layers, π_j , are related through the interface perturbation η as usual,

$$\pi_2 - \pi_1 + s(\pi_2 + \pi_1) = \text{Bu} \eta, \quad (6.3)$$

and $s = (\rho_2 - \rho_1)/(\rho_2 + \rho_1)$ is the stratification parameter, $\text{Bu} = (R_d/r_0)^2$ is the Burger number, $\text{Ro} = \Delta\Omega/(2\Omega)$ is the Rossby number (as used in experiments, cf. Flór *et al.* [2011]), $R_d = (g' H_0)^{1/2}/(2\Omega)$ is the Rossby deformation radius, and $g' = 2 \Delta\rho g/(\rho_1 + \rho_2) = 2sg$ is the reduced gravity.

The depth profiles $H_j(r)$ and respective velocities $V_j(r)$ in (6.2) correspond to a steady cyclogeostrophically balanced state of the two-layer system that obeys the nondimensional equations.

$$V_j + \frac{V_j^2}{r} + \frac{r}{4} = \partial_r \Pi_j, \quad (6.4)$$

where the $r/4$ term corresponds to the centrifugal effect at the interface, while the other terms correspond to the classical cyclogeostrophic equilibrium.

The rotation rates of the layers lie in the interval between the rotation rate of the base (0 in the rotating frame) and that of the upper lid (Ro in the rotating frame). Therefore, in general,

$$V_2 = \alpha_2 r, \quad V_1 = \alpha_1 r \quad (6.5)$$

and we get the following expressions for the heights of the layers in the state of cyclogeostrophic equilibrium for such mean flow:

$$\begin{aligned} H_j &= H_j(0) + (-1)^j [\alpha_2 + \alpha_2^2 - \alpha_1 - \alpha_1^2] \frac{r^2}{2 \text{Bu}} \\ &+ (-1)^j s [\alpha_2 + \alpha_2^2 + \alpha_1 + \alpha_1^2 + 1/2] \frac{r^2}{2 \text{Bu}}. \end{aligned} \quad (6.6)$$

Hart [1972] considered the top, bottom, and interfacial friction layers and found that the rotation rates are $\alpha_1 = (2 + \chi) \text{Ro}/2(1 + \chi)$ and $\alpha_2 = \text{Ro}/2(1 + \chi)$, where $\chi = (\nu_2/\nu_1)^{1/2}$ is the viscosity ratio between the two layers. If the two layers have close viscosities $\chi = 1$, it leads to $(\alpha_1, \alpha_2) = (0.75 \text{Ro}, 0.25 \text{Ro})$.

A calculation based on a layerwise balance of the torques in *Williams et al.* [2004] gives values for (α_1, α_2) of the same order but depending on the turntable angular velocity. The direct measurements of the radial velocity profiles by *Flór* [2007] are closer to $(\alpha_1, \alpha_2) \approx (0.9 \text{Ro}, 0.1 \text{Ro})$. We will therefore keep these last values throughout the chapter, but this particular choice means no loss of generality, as changing the relative rotation rate just means rescaling the Rossby number.

Supposing a harmonic form of the solution in the azimuthal direction,

$$\begin{aligned} & (u_j(r, \theta), v_j(r, \theta), \pi_j(r, \theta)) \\ &= (\tilde{u}_j(r), \tilde{v}_j(r), \tilde{\pi}_j(r)) \exp[ik(\theta - ct)] + \text{c.c.}, \quad (6.7) \end{aligned}$$

where k is the azimuthal wave number ($k \in \mathbb{N}$), and omitting tildes we get, from (6.2),

$$\begin{aligned} & k(V_j - rc)iu_j - (r + 2V_j)v_j + r\partial_r\pi_j = 0, \\ & -(r + V_j + r\partial_r(V_j))iu_j + k(V_j - rc)v_j + k\pi_j = 0, \\ & -\partial_r(rH_jiu) + kH_jv + k(V_j - rc)(-1)^j\eta = 0, \\ & \pi_2 - \pi_1 + s(\pi_2 + \pi_1) = \text{Bu} \eta. \quad (6.8) \end{aligned}$$

The system (6.8) is an eigenproblem of order 6 that can be solved by applying the spectral collocation method [*Trefethen*, 2000].

The dispersion diagrams we thus obtain show that the branches of dispersion relation corresponding to different modes can intersect, leading to linear wave resonances and thus creating instabilities of various nature [*Cairns*, 1979; *Sakai*, 1989].

Following *Cairns* [1979] and *Ripa* [1983], the flow with velocity U_0 is unstable if there exists a pair of waves with intrinsic frequencies $\tilde{\omega}_1$ and $\tilde{\omega}_2$ that satisfy the following conditions: The waves propagate in the opposite directions with respect to the basic flow $\tilde{\omega}_1\tilde{\omega}_2 < 0$, meaning that they have opposite energy anomalies, and have almost the same Doppler-shifted (absolute) frequencies ($\tilde{\omega}_1 + kU_0 \sim \tilde{\omega}_2 - kU_0$) and thus can phase lock and resonate. The interpretation of the unstable modes as resonances between the neutral waves provides a classification of different instabilities and corresponding regions of parameter space.

Namely, we will display below the instabilities resulting from the resonance between Rossby waves in upper

and lower layers (the baroclinic instability), the resonance between Rossby and Kelvin or Poincaré waves in respective layers (Rossby-Kelvin instability), and the resonances between two Poincaré, or Kelvin and Poincaré, or two Kelvin modes (Kelvin-Helmholtz shear instability). We should recall at this point the physical nature of different waves in the two-layer shallow-water system: Rossby waves propagate due to potential vorticity gradients, whatever their origin, Kelvin waves propagate due to (and along) the boundaries in the rotating systems, and Poincaré waves are inertia-gravity waves propagating due to the density jump at the interface or at the free surface. Although each instability occupies its proper domain in the parameter space, we will see that there exist crossover regions where two different instabilities coexist and may compete.

6.2.2. Instabilities and Growth Rates

We first present the overall stability diagram in the space of parameters of the model and then illustrate different parts of this diagram by displaying the corresponding unstable modes and dispersion curves. The stability diagram was obtained by calculating the eigenmodes and the eigenvalues of the problem (6.5), (6.8) for about 50,000 points in the space of parameters (there are typically 200–300 points along each axis in the figures below) and then interpolating. Only discrete azimuthal wave numbers correspond to realizable modes. We nevertheless present the results as if the spectrum of wave numbers were continuous for better visualization. They are synthesized in Figures 6.2 and 6.3 displaying the growth rates and the wave numbers, respectively, of the most unstable modes. Both figures represent the plane of parameters Ro-Bu (Figures 6.2 and 6.3). We also show in Figure 6.4 how the dispersion diagrams evolve while changing parameters and approaching the instability band spreading from low left to upper right in Figures 6.2 and 6.3. One clearly sees how the initially stable flow without imaginary eigenvalues of c develops instabilities of various nature as parameters change. Thus, as shown in the left column of Figure 6.4, decreasing the Burger number leads to distortion of the dispersion curves of Rossby modes and their reconnection leading to Rossby-Rossby (RR) resonance, i.e., the baroclinic instability. Different distortion of dispersion curves of Rossby modes takes place if Ro increases at constant Bu , leading to reconnection with (a) a Kelvin-mode curve and Rossby-Kelvin (RK) resonance with corresponding instability and (b) a Poincaré-mode curve and Rossby-Poincaré (RP) resonance and corresponding instability. Further increase in Ro leads to reconnection of Kelvin-mode curves and Kelvin-Kelvin (KK) resonance and related shear instability with features

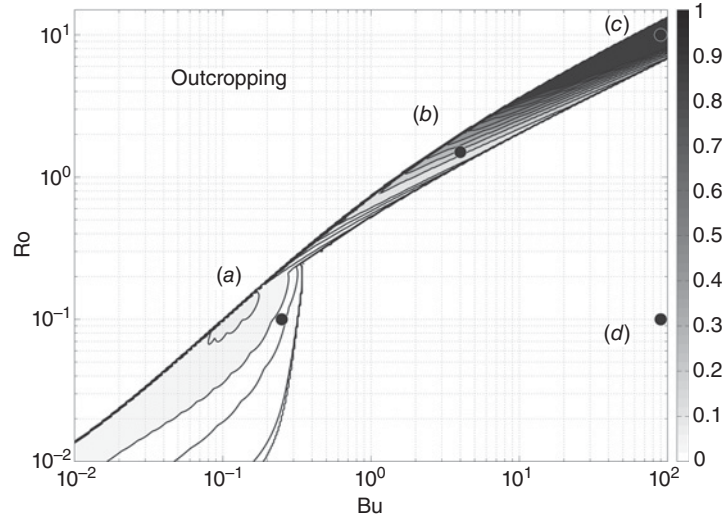


Figure 6.2. Growth rate of most unstable modes in (Ro, Bu) space. Darker zones correspond to higher growth rates. Contours displayed are 0.001, 0.01, 0.02 and further interval at 0.02. The thick upper frontier line marks the outcropping limit when the interface between the two layers intersects the bottom or the top. Adapted from *Gula et al.* [2009b].

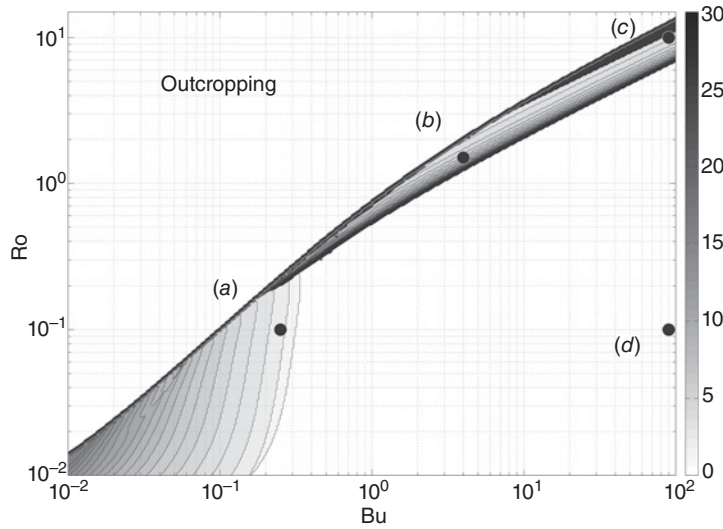


Figure 6.3. Wave number of most unstable modes in (Ro, Bu) space corresponding to Figure 6.2. Darker zones correspond to higher wave numbers. The interval between subsequent contours is 1. Adapted from *Gula et al.* [2009b].

similar to the classical Kelvin-Helmholtz (KH) instability [*Paldor and Ghil, 1991*]. Note that although KK, Kelvin-Poincaré (KP), and Poincaré-Poincaré (PP) resonances are physically different, they are frequently confused in the literature and appear under the general name of KH instability. Similarly RK and RP instabilities are often both called RK [cf. *Sakai, 1989*]. We follow this simplified convention.

In the context of wave resonances, there are three essential parameters in the problem: $V = \Delta\Omega r_0$, the velocity

(or velocity shear) of the basic flow; $C_R = \Omega \Delta H / H_0 r_0$, the characteristic phase velocity of the Rossby waves; and $C_G = \sqrt{g' H_0}$, the characteristic phase velocity of the gravity waves. The interpretation of the results may be done on the basis of the alternative set of nondimensional parameters defined as

$$F^* = \frac{V}{C_G} = \frac{\Delta\Omega r_0}{\sqrt{g' H_0}},$$

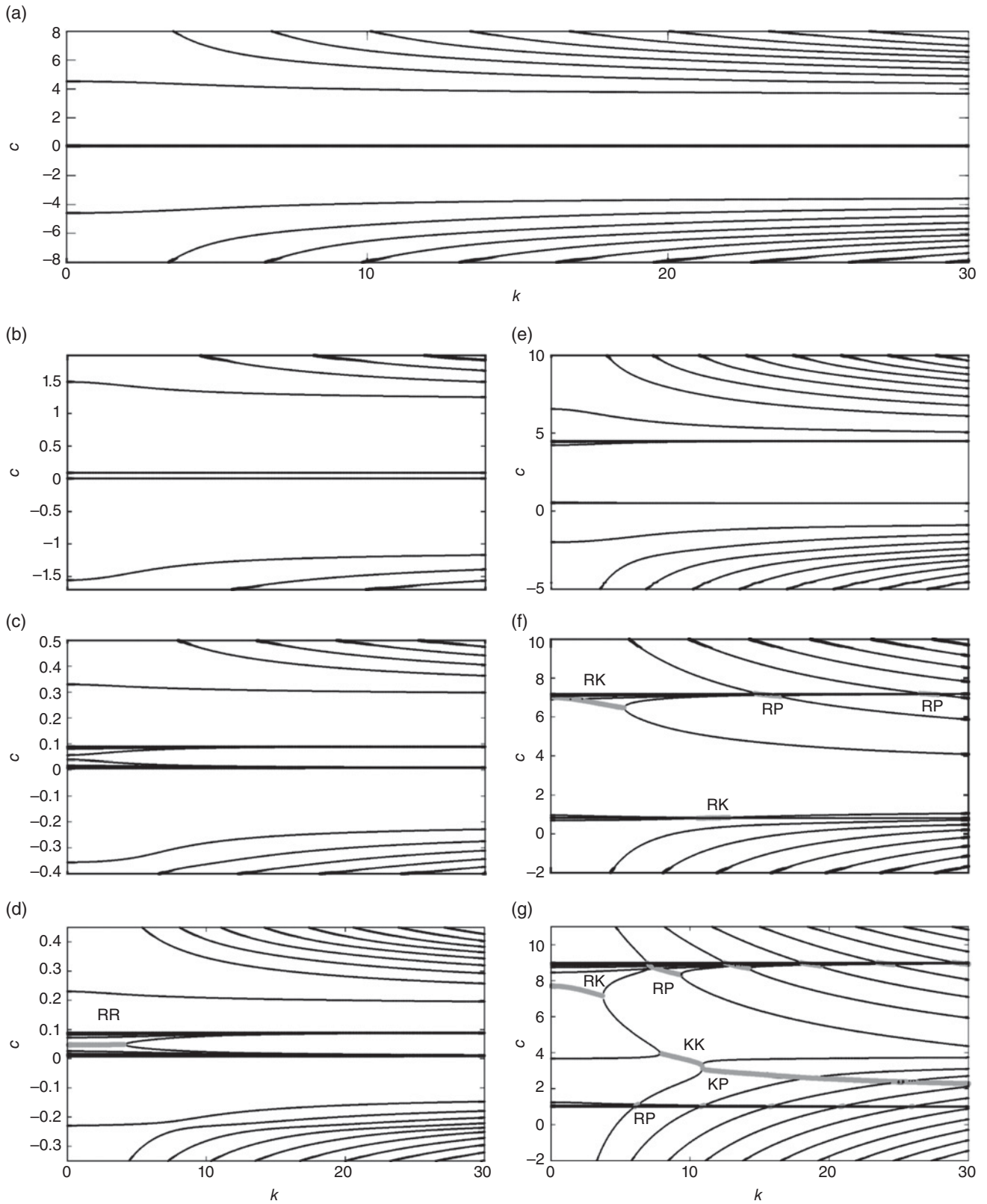


Figure 6.4. Dispersion diagram $c-k$ for the stable configuration corresponding to point (d) in Figure 6.2 (upper panel) and its evolution with the change of parameters: $Ro = 0.1$, Bu decreasing from top to bottom. Left panel: (a) $Bu = 90$, (b) $Bu = 10$, (c) $Bu = 0.5$, and (d) $Bu = 0.25$. $Bu = 90$, Ro increasing from top to bottom. Right panel: (a) $Ro = 0.1$, (e) $Ro = 5$, (f) $Ro = 8$, and (g) $Ro = 10$. Thick gray lines correspond to unstable regions; nonzero $\text{Im}(c)$. Adapted from Gula *et al.* [2009b].

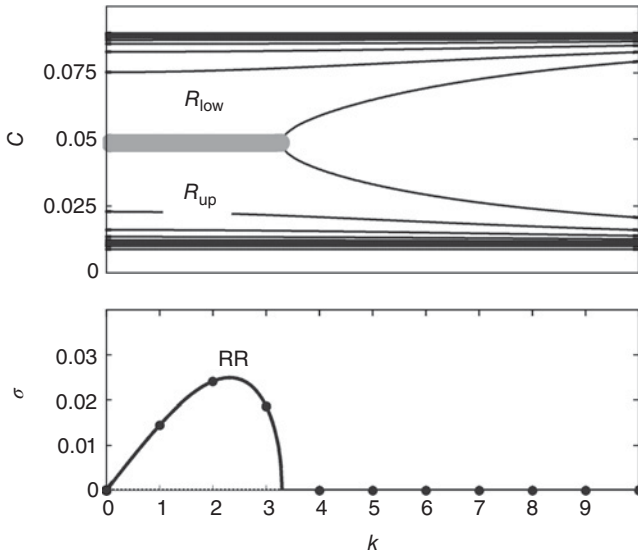


Figure 6.5. Dispersion diagram (upper panel) and growth rate (lower panel) of the eigenmodes of the superrotating lid configuration for $Ro = 0.1$ and $Bu = 0.25$ (see Figure 6.2a). Thick gray line in the upper panel corresponds to the RR resonance and respective unstable modes. Here and subsequent figures the subscripts “low” and “up” indicate a wave in the lower and upper layer, respectively.

the Froude number, and

$$R^* = \frac{V}{C_R} = \frac{g'H}{2\Omega^2 r_0^2},$$

a new Rossby number. With these definitions one finds the baroclinic instability at small R^* and KH instabilities at large F^* , which matches the traditional view of these instabilities. However, to keep a closer link with experimental results of *Williams et al.* [2005] and *Flór et al.* [2011], the discussion below is based on Bu and Ro . (For more details, see *Gula et al.* [2009b].)

Thus, as for the ageostrophic Phillips model in a straight channel [cf. *Sakai*, 1989; *Gula et al.*, 2009a], several types of instabilities are present, namely, (a) the baroclinic instability for small values of Bu and Ro (RR resonance), (b) the Rossby-Kelvin instability (RK or RP resonance) for intermediate values of Bu and Ro , and (c) the Kelvin-Helmholtz instability (KK or KP resonance) for high values of Bu and Ro . As usual, the KH instability is characterized by highest growth rates and shortest wavelengths, the baroclinic instability is long-wave and low growth-rate, and RK instability is intermediate, although spanning a wide range of wave numbers.

In Figures 6.5–6.7 we give the dispersion diagrams corresponding to different values of (Ro, Bu) referring to typical cases (a), (b), (c), respectively, in Figures 6.2 and 6.3.

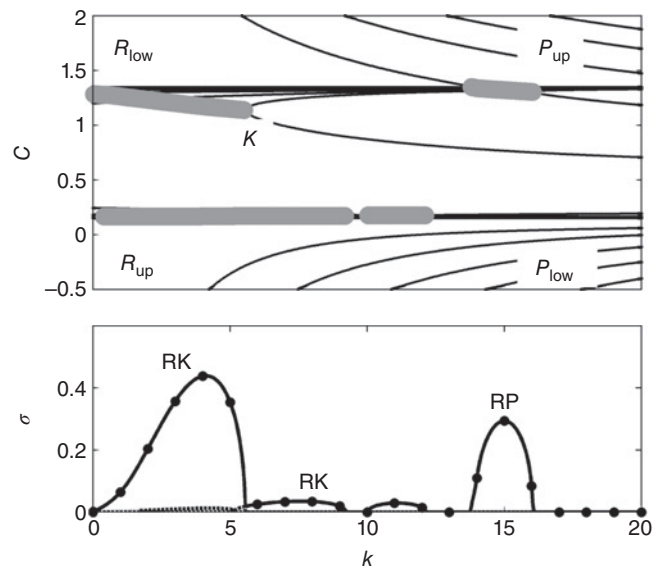


Figure 6.6. Dispersion diagram (upper panel) and growth rate (lower panel) of the eigenmodes of the superrotating lid configuration for $Ro = 1.5$ and $Bu = 3.5$ (see Figure 6.2b). Thick gray lines on the upper panel correspond to the RK and RP resonances and respective unstable modes.

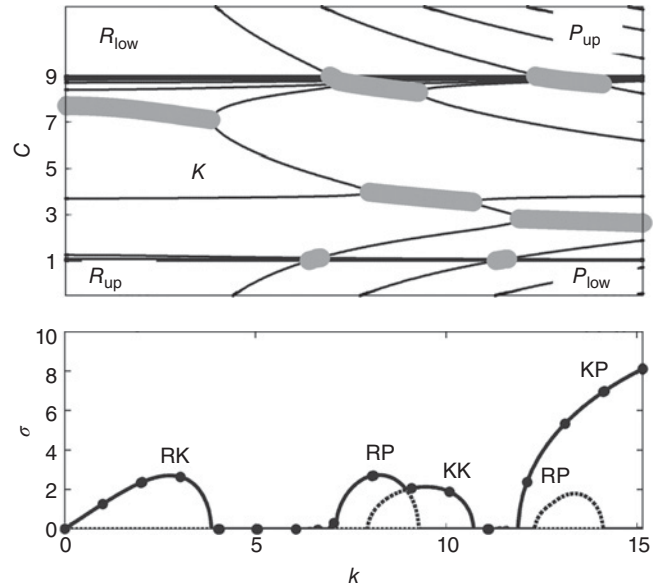


Figure 6.7. Dispersion diagram (upper panel) and growth rate (lower panel) of the eigenmodes of the superrotating lid configuration for $Ro = 10$ and $Bu = 90$ (see Figure 6.2c). Thick gray lines on the upper panel correspond to the RK, KK, RP, and KP resonances and respective unstable modes.

We present also in Figure 6.8 the structure of unstable modes in both layers and the corresponding maps of the interface deviation, which is an often measured quantity in experiments.

Figure 6.5 shows a dispersion diagram in the zone of baroclinic instability. Two Rossby waves, one propagating in each layer, are in resonance having the same Doppler-shifted phase speed and giving rise to a baroclinic instability, as explained, e.g., in *Hoskins et al.* [1985]. The structure of the unstable mode is shown in Figure 6.8a.

Figure 6.6 shows a dispersion diagram in the Rossby-Kelvin instability area. The gravest radial Rossby mode propagating in the upper layer resonates with a Kelvin wave propagating in the lower layer and gives rise to the dominant RK instability; see *Sakai* [1989] and *Gula et al.* [2009a]. Resonances of higher Rossby modes with the Kelvin wave give weaker RK instabilities, and the resonance of a lower-layer Rossby mode with a Poincaré wave gives the RP instability. The structure of the most unstable RK and RP modes is shown in Figures 6.8b and 6.8c.

Figure 6.7 shows a dispersion diagram in a KH instability area. A Kelvin wave propagating in the upper layer resonates with another Kelvin wave propagating in the lower layer and gives rise to a KH instability. For these values of parameters we can see that RP and RK instabilities

are also present but with lower growth rates. The structure of an unstable KK mode is shown in Figure 6.8d.

Thus RK and KH instabilities coexist for large Bu and Ro having comparable growth rates although different characteristic wave numbers. As follows from Figure 6.7 and from the comparison of Figures 6.2 and 6.3, in general, close values of the growth rates may correspond to essentially different wavelengths of the most unstable modes. This means that different instabilities may coexist and compete.

6.3. STABILITY OF OUTCROPPING BUOYANCY-DRIVEN BOUNDARY CURRENTS

6.3.1. Equations of Motion, Basic States, Linearization and Boundary Conditions

Another configuration used in experiments with the rotating annulus is the free surface-outcropping one [*Griffiths and Linden, 1982; Pennel et al., 2012*]. Note that outcropping was excluded in the analysis of the previous

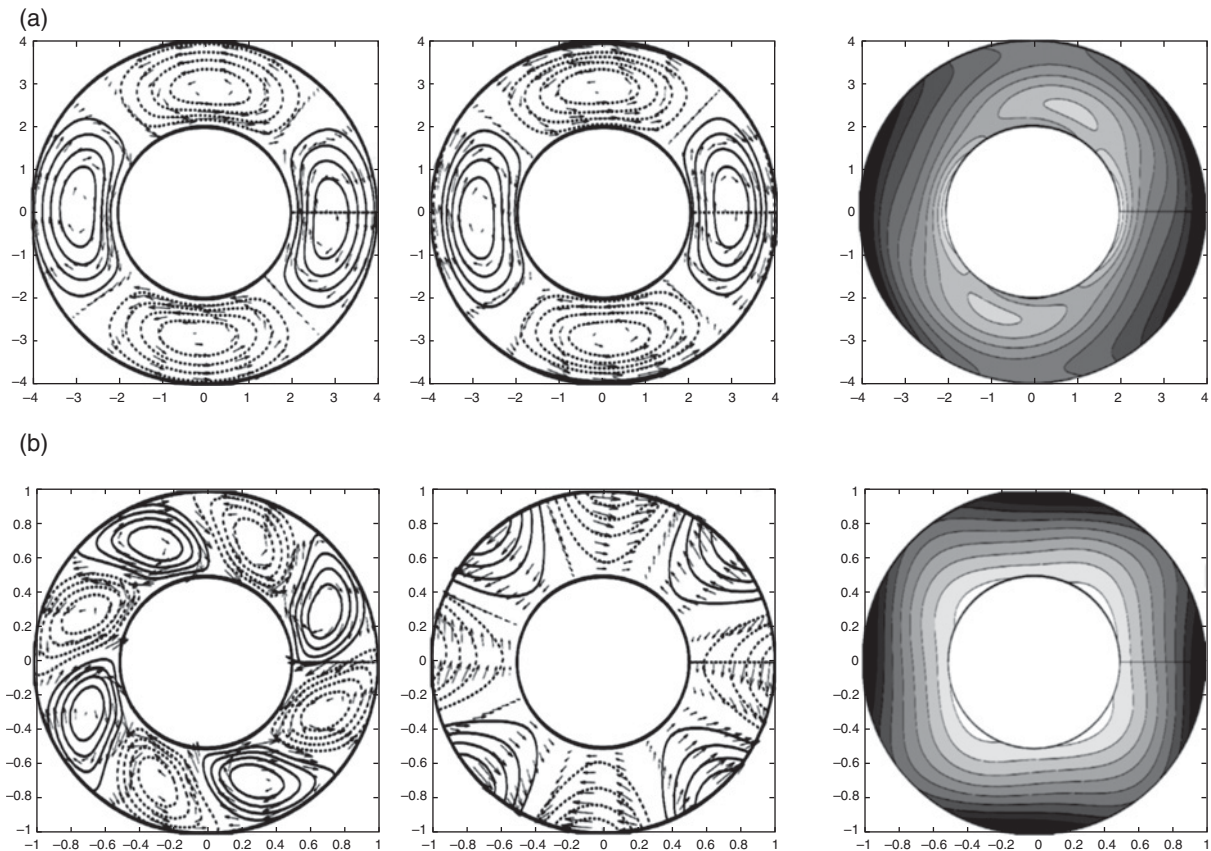


Figure 6.8. Pressure and velocity fields in the upper (left) and lower (middle) layers and interface height (right) of (a) the baroclinically unstable RR mode at $k = 2$ ($kR_d = 0.9$, see Figure 6.5), (b) the unstable RK mode at $k = 4$ ($kR_d = 7.5$, see Figure 6.6),

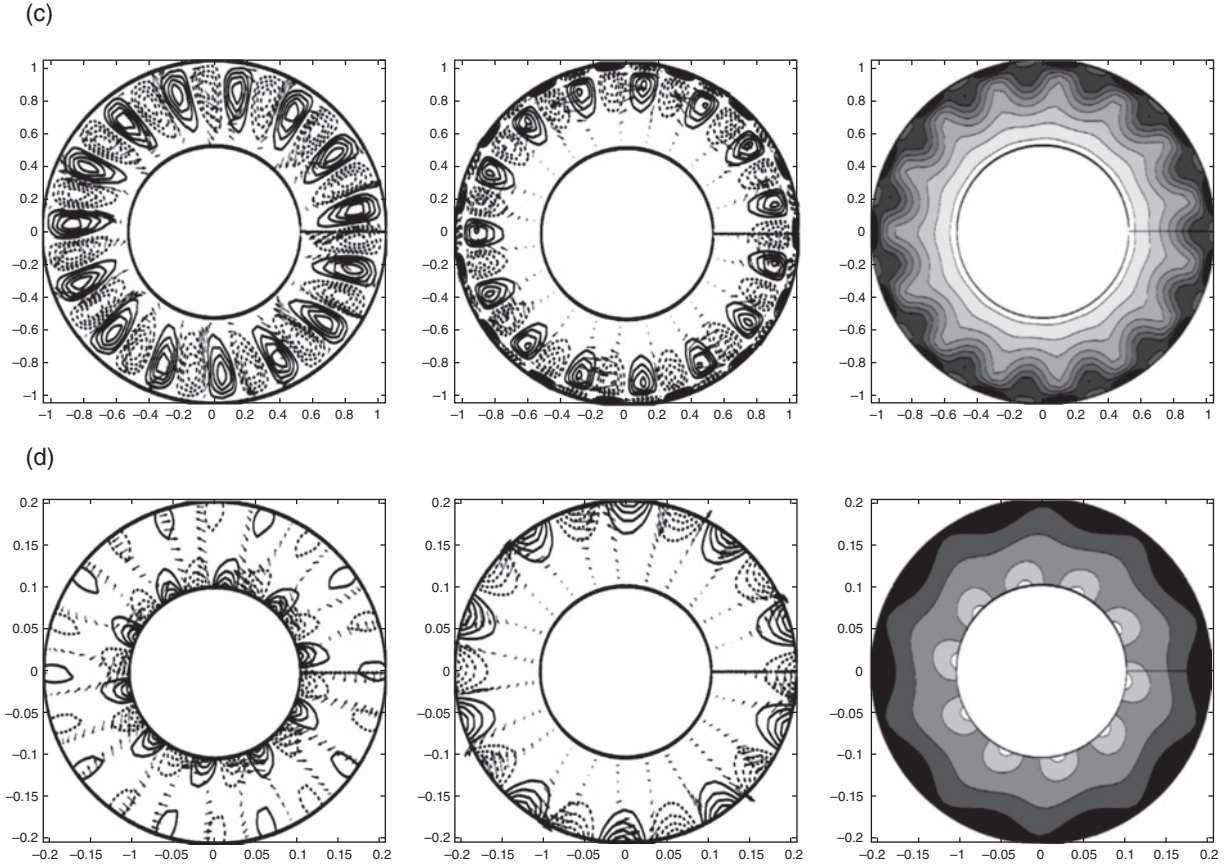


Figure 6.8 Continued. (c) the unstable RP mode at $k = 15$ ($kR_d = 28$, see Figure 6.6), and (d) the unstable KK mode at $k = 10$ ($kR_d = 95$, see Figure 6.7). The full lines correspond to positive and the dotted lines to negative values. (a) Both fields are typical of a Rossby mode. (b) The field in the upper layer is typical of a Rossby mode while the field in the lower layer is typical of a Kelvin mode. (c) The field in the upper layer is typical of a Rossby mode while the field in the lower layer is typical of a Poincaré mode. (d) Both fields are typical of a Kelvin mode.

section. So we consider now the situation where the interface between the layers joins the free surface forming a surface front, as shown in Figure 6.9. This is an idealized configuration of a buoyancy-driven coastal current in a circular basin. In the classical experiments by *Griffiths and Linden* [1982], a volume of lighter salty water of density ρ_1 flows above a denser water of density ρ_2 and is confined between the surface front and the internal cylinder. In the work of *Thivolle-Cazat and Sommeria* [2004] and *Pennel et al.* [2012], the lighter fluid flows along the external cylinder. In the following we consider an upper layer of lighter fluid of density ρ_1 with a free surface terminating at a point $r = r_0 = r_1 + L$ with mean velocity $U_1(r)$ and a lower layer of density $\rho_2 > \rho_1$ with a mean velocity $U_2(r)$.

We work with the two-layer shallow-water equations in the cylindrical geometry, as in the previous section, and perform a cylindrical equivalent of the stability analysis of *Gula and Zeitlin* [2010] and *Gula et al.* [2010] for

coastal currents. Another difference with the previous section is that we now consider a free surface instead of a rigid lid for the comparison with experiments. In this section the slope of the bottom, γ , is set to be zero, its influence to be studied in the next section.

By introducing the time scale $1/f$, the horizontal scale L , which is the unperturbed width of the density current, the vertical scale $H_0 = H_1(r_1)$, and the velocity scale fL , we use nondimensional variables from now on without changing notation. Note that with this scaling the characteristic value of the velocity gives the Rossby number. By linearizing about a steady state in cyclogeostrophic equilibrium, we obtain nondimensional equations identical to equations (6.2), where the pressure perturbations in the layers π_j are now related through the layers' heights h_j via the hydrostatic relations as follows:

$$\nabla \pi_j = \frac{\text{Bu}}{2s} \nabla (\delta_s^{j-1} h_1 + h_2). \quad (6.9)$$

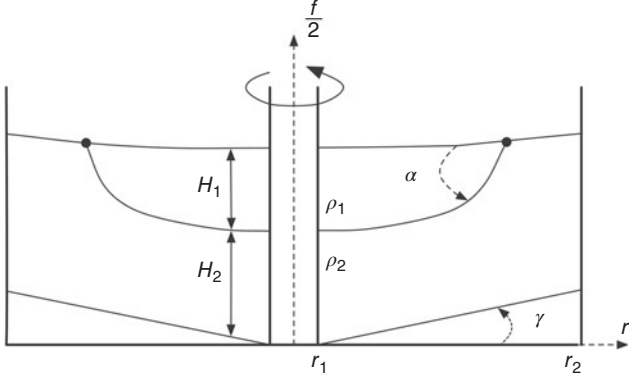


Figure 6.9. Schematic representation of a two-layer outcropping flow in the annulus with linearly sloping bottom.

Here $\delta_s = \rho_1/\rho_2$ is the density ratio, $s = (\rho_2 - \rho_1)/(\rho_2 + \rho_1)$ is the stratification parameter, and $\text{Bu} = (R_d/r_0)^2$ the Burger number.

The depth profiles $H_j(r)$ and respective velocities $V_j(r)$ in (6.2) correspond to steady cyclogeostrophically balanced states in each layer:

$$V_j + \frac{V_j^2}{r} + \frac{r}{4} = \frac{\text{Bu}}{2s} \partial_r (\delta_s^{j-1} H_1 + H_2). \quad (6.10)$$

We look for solutions harmonic in the azimuthal direction:

$$(u_j(r, \theta), v_j(r, \theta), \pi_j(r, \theta)) = (\tilde{u}_j(r), \tilde{v}_j(r), \tilde{\pi}_j(r)) \exp [ik(\theta - ct)] + \text{c.c.} \quad (6.11)$$

The boundary condition of no normal flow at the coast is the same as in the previous case for both layers, $u_j(r_1) = 0$. The boundary conditions at the front for the upper layer are

$$H_1(r) + h_1(r, \theta, t) = 0, \quad D_t L_R = v \quad \text{at } r = L_R(\theta), \quad (6.12)$$

where $r = r_1 + L$ is the location of the free streamline of the basic state, $L_R(\theta, t)$ is the position of the perturbed free streamline, and $D_t = \partial_t + u \partial_r + v/r \partial_\theta$ is the Lagrangian derivative. Physically, they correspond to the conditions that the fluid terminates at the boundary, which is a material line. The linearized boundary conditions give (1) the relation between the perturbation of the position of the free streamline and the value of the height perturbation,

$$L_R = - \frac{h_1}{H_{1r}} \Big|_{r=r_1+L}, \quad (6.13)$$

and (2) the continuity equation evaluated at $r = r_1 + L$. Hence, the only constraint to be imposed at the front for the upper layer is the regularity of $(u_1, v_1, h_1 + h_2)$.

We also have to ensure the continuity of pressure of the lower layer across the front. In the region $r > r_1 + L$ with no upper layer, the lower layer obeys the one-layer rotating shallow-water equations with (hydrostatic) pressure proportional to the height of the fluid column. In what follows we consider an outer cylinder to be far enough from the front ($r_2 \gg r_0$) so that its influence is negligible. Moreover, below we will limit ourselves, for technical simplicity, only by the *balanced* component of π_2 , which, in the leading order, in polar coordinates, satisfies the equation [cf., e.g., *Reznik et al.*, 2001]

$$\frac{1}{r} \partial_r (r \partial_r \pi_2) + \left(k^2 - \frac{1}{R_{d2}^2} - \frac{k^2}{r^2} \right) \pi_2 = 0, \quad (6.14)$$

where $R_{d2} = \sqrt{gH_2}/f$ is the Rossby deformation radius of the lower layer. We thus impose the continuity of the full solution for π_2 in the inner region, $r < r_1 + L$, with the decaying balanced solution in the outer region, $r > r_1 + L$, at $r = r_1 + L$. By this choice an unbalanced part of the one-layer flow beyond the front, consisting of freely propagating surface inertia-gravity waves, is discarded. We thus loose possible resonances of the eigenmodes of the inner flow with the outer inertia-gravity wavefield and related radiative instabilities. For small to moderate Rossby numbers, which is the case of existing experiments, and our case below, these instabilities are weak [cf. *Zeitlin*, 2008]. As we will see later, the stability analysis under these assumptions reproduces the experiments well, which gives an a posteriori justification.

Injecting (6.11) into (6.2) and (6.9), we obtain an eigenvalue problem of order 6 that can be solved by applying the spectral collocation method along the same lines as in the previous section. In what follows, we will first consider the simplest case of a bottom layer initially at rest ($U_2 = 0$) and an upper flow with a constant rotation rate $U_1 = \alpha r$.

6.3.2. Resonances and Instabilities

As in the configuration of Section 6.2, the instabilities in the outcropping case originate from resonances between the eigenmodes of the linearized problem. As in the previous section, the wave species are Poincaré (inertia-gravity) modes, Rossby modes (if PV gradients are present), and unidirectional Kelvin modes trapped at the boundary. Additional ingredients in the outcropping configuration are the frontal modes trapped in the vicinity of the free streamlines (outcropping lines). These modes are described in *Iga* [1993] as mixed Rossby-gravity waves

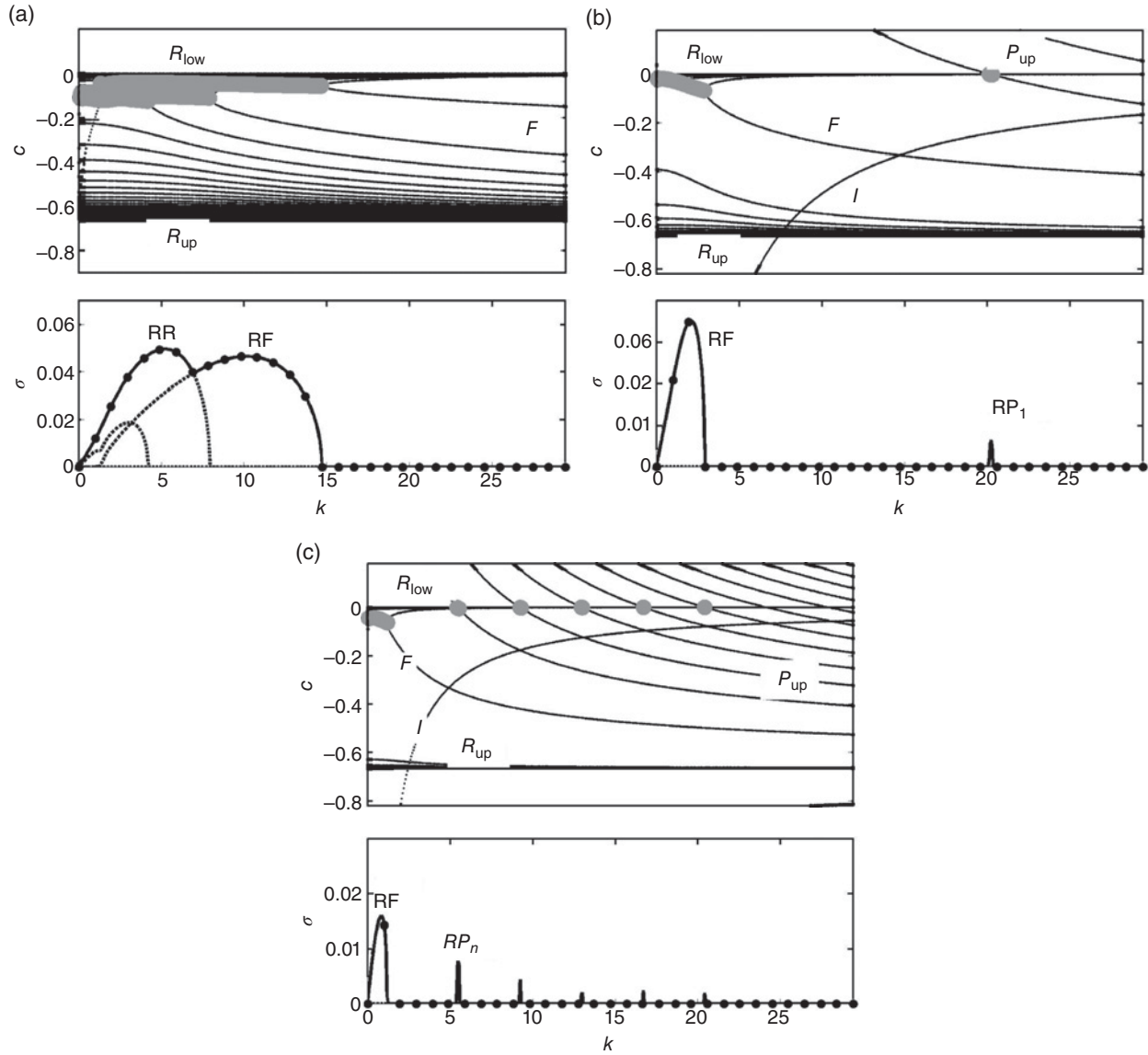


Figure 6.10. Dispersion diagram (upper panels) and growth rate (lower panels) of the eigenmodes of the outcropping configuration for (a) $Ro = 0.02$, (b) $Ro = 0.2$, and (c) $Ro = 0.6$ with $\delta_H = 0.1$. Thick gray lines on the upper panel correspond to the unstable modes.

in the sense that they behave like Rossby modes as long as the wave number is small and like gravity modes when the wave number becomes large. Note that *Hayashi and Young* [1987] and other authors refer to these modes as Kelvin waves, as they propagate along the (internal) boundary. More generally, the frontal mode can be interpreted as a vortical mode, as in the work of *Meacham and Stephens* [2001], *Gula and Zeitlin* [2010], and *Gula et al.* [2010], in a sense of a wave that exists due to the PV gradient at the outcropping point, because this point may be interpreted as a point connecting the finite-depth layer with

a layer of infinitesimal thickness [*Boss et al.*, 1996]. We use the denomination “frontal” for such modes in what follows.

Figure 6.10 shows the dispersion diagram and corresponding growth rates of the eigenmodes of the outcropping coastal flow with a depth ratio $\delta_H = H_1(r_1)/[H_1(r_1) + H_2(r_1)] = 0.1$ and a density ratio $\delta_s = \rho_1/\rho_2 = 0.99$ as a function of k for increasing values of vertical shear: $Ro = 0.02$, $Ro = 0.2$, and $Ro = 0.6$.

For low Rossby and Burger numbers (Figure 6.10a), Rossby modes in the lower layer with $c \approx U_2 = 0$ can

resonate with Rossby modes in the upper layer with $c \approx -U_0$. This is the standard mechanism of the baroclinic instability, as explained in the previous section, which occurs for wave numbers $kR_d < 1$. The corresponding pressure and velocity fields in both layers are plotted in Figure 6.11a. Both fields are typical of a Rossby mode. Rossby modes in the lower layer can also resonate with the frontal mode in the upper layer (RF interaction). The frontal mode has the characteristics of a Rossby wave for low wave numbers, and the unstable mode under consideration is therefore very similar to the classical baroclinic instability (RR). The corresponding pressure and velocity fields in both layers are plotted in Figure 6.11b.

For higher Rossby and Burger numbers (Figures 6.10b and 6.10c), the Rossby-Rossby interaction is not allowed anymore as the horizontal extension of the surface current is too small compared to the Rossby deformation radius. The RF mode is the primary unstable mode with wave numbers $kR_d \approx 0.5 \div 1$. The second instability

in Figure 6.10b corresponds to the first Poincaré mode in the upper layer resonating with a Rossby wave in the lower layer. The pressure and velocity fields for this mode are plotted in Figure 6.11c, and confirm this interpretation. Note that the same instability appears at higher k for Poincaré modes of higher order with decreasing growth rates (Figure 6.10c). This is the RP instability.

A new dispersion curve $kc = 1$ denoted by I in the Figures 6.10b and 6.10c also appears. It corresponds to inertial motion in the lower layer, with the quiescent upper layer. The absence of pressure variations is typical for inertial oscillations. This mode was already discussed by *Paldor and Ghil* [1991] and *Gula et al.* [2010]. In spite of intersections of this curve with other branches of the dispersion diagram, no resonances and hence no instabilities between the inertial motion and other modes arise due to its pressureless character. Indeed, pressure fluctuations are required for the instability to arise [*Cairns,*

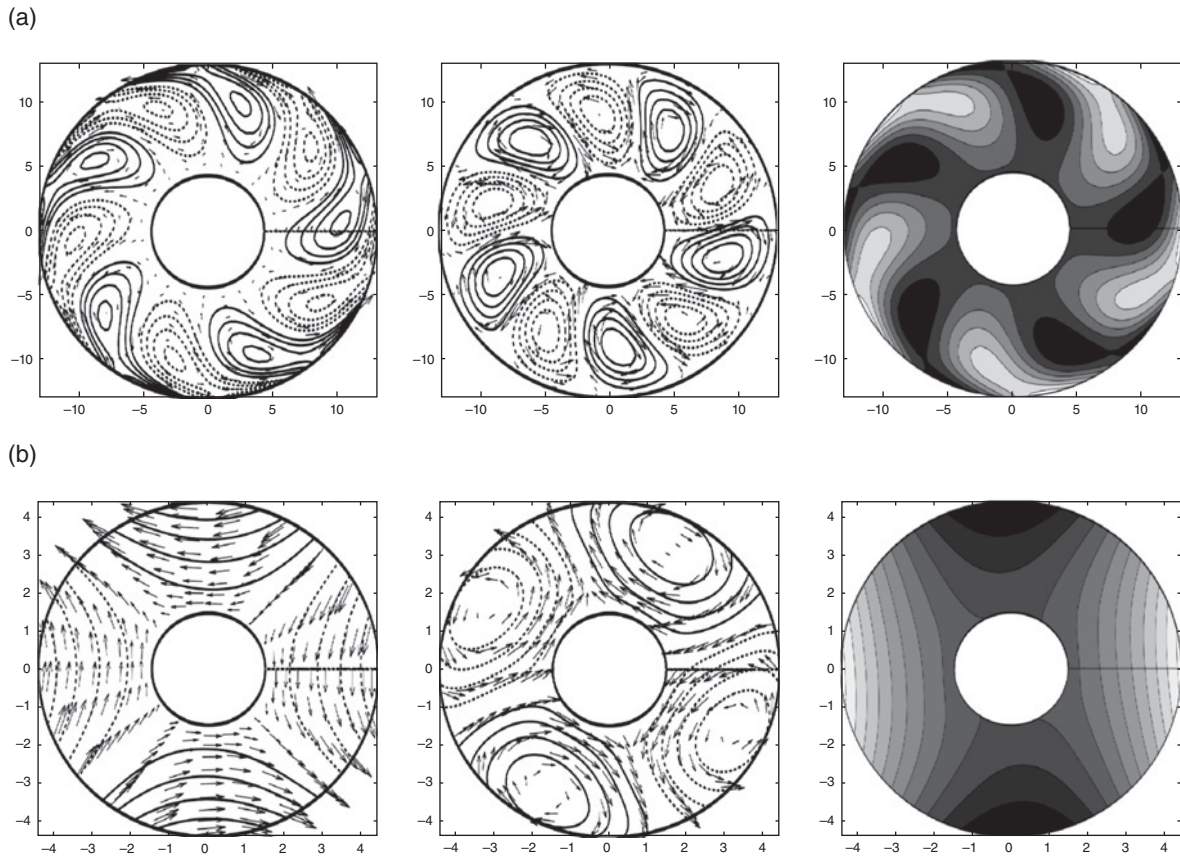
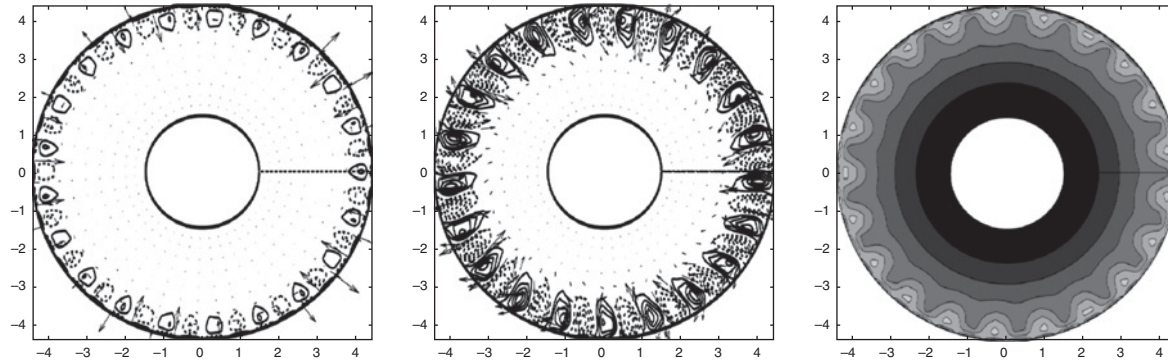


Figure 6.11. Pressure and velocity fields of the upper (left) and lower (middle) layers and interface height (right) of (a) the unstable RR mode for $Ro = 0.02$ and $k = 5$ ($kR_d = 0.6$, see Figure 6.10a), (b) the unstable Rossby-frontal (RF) mode for $Ro = 0.2$ and $k = 2$ ($kR_d = 0.6$, see Figure 6.10b),

(c)



(d)

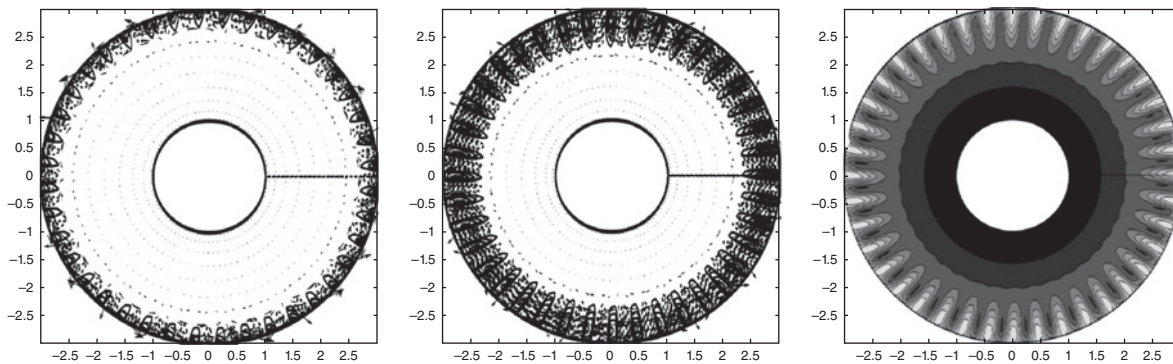


Figure 6.11 Continued. (c) the unstable RP mode at $k = 21$ ($kR_d = 7.5$, see Figure 6.12b), and (d) the unstable frontal-Poincaré mode at $k = 40$ ($kR_d = 23$, see Figure 6.10c). Full lines: positive; dotted lines: negative values.

1979] as the coupling between the layers, necessary for the resonance between upper and lower layer waves, is achieved through pressure (cf. the instability criterion in Sakai [1989]).

It should be emphasized that resonances involving the Kelvin mode at the inner boundary, in contradistinction with the previous section and the results of Gula and Zeitlin [2010] and Gula *et al.* [2010], are never of significant impact in the present configuration, where the vertical shear at the inner cylinder is small compared to the shear at the location of the front.

Figure 6.12 shows the dispersion diagram and corresponding growth rates for a larger depth ratio $\delta_H = H_1(r_1)/[H_1(r_1) + H_2(r_1)] = 0.5$ and a density ratio $s = \rho_1/\rho_2 = 0.99$. Comparison of Figures 6.10 and 6.12 shows that the unstable modes become more and more vigorous when the depth ratio increases. For high Rossby numbers, a new zone of instabilities with high growth rates appears at very high wave numbers. They are due to the interaction of the frontal mode in the upper layer with various Poincaré modes in the lower layer (FP_1). Such short-wave

instability is analogous to the one described by Paldor and Ghil [1991] for the zero-PV case and by Gula *et al.* [2010] for the constant-PV case in the planar geometry. The frontal mode having the characteristics of a gravity wave for high wave numbers, this instability is therefore very similar to the vertical shear instabilities, which we have seen previously (KK, KP, or PP). The pressure and velocity fields for the first Poincaré mode in the lower layer and the frontal mode in the upper layer are plotted in Figure 6.11d.

Barotropic interactions in the upper layer, as studied by Gula and Zeitlin [2010] in the rectilinear case, are not present in this analysis due to the absence of both horizontal potential vorticity gradient and current reversal in the upper layer, which would allow Rossby-Frontal or Kelvin-Frontal barotropic interactions, respectively. These interactions are usually absent in experimental studies, as mentioned above, due to the lack of surface forcing, which would allow for stronger horizontal shear in the equilibrium state. Experiments realized through geostrophic adjustment of a

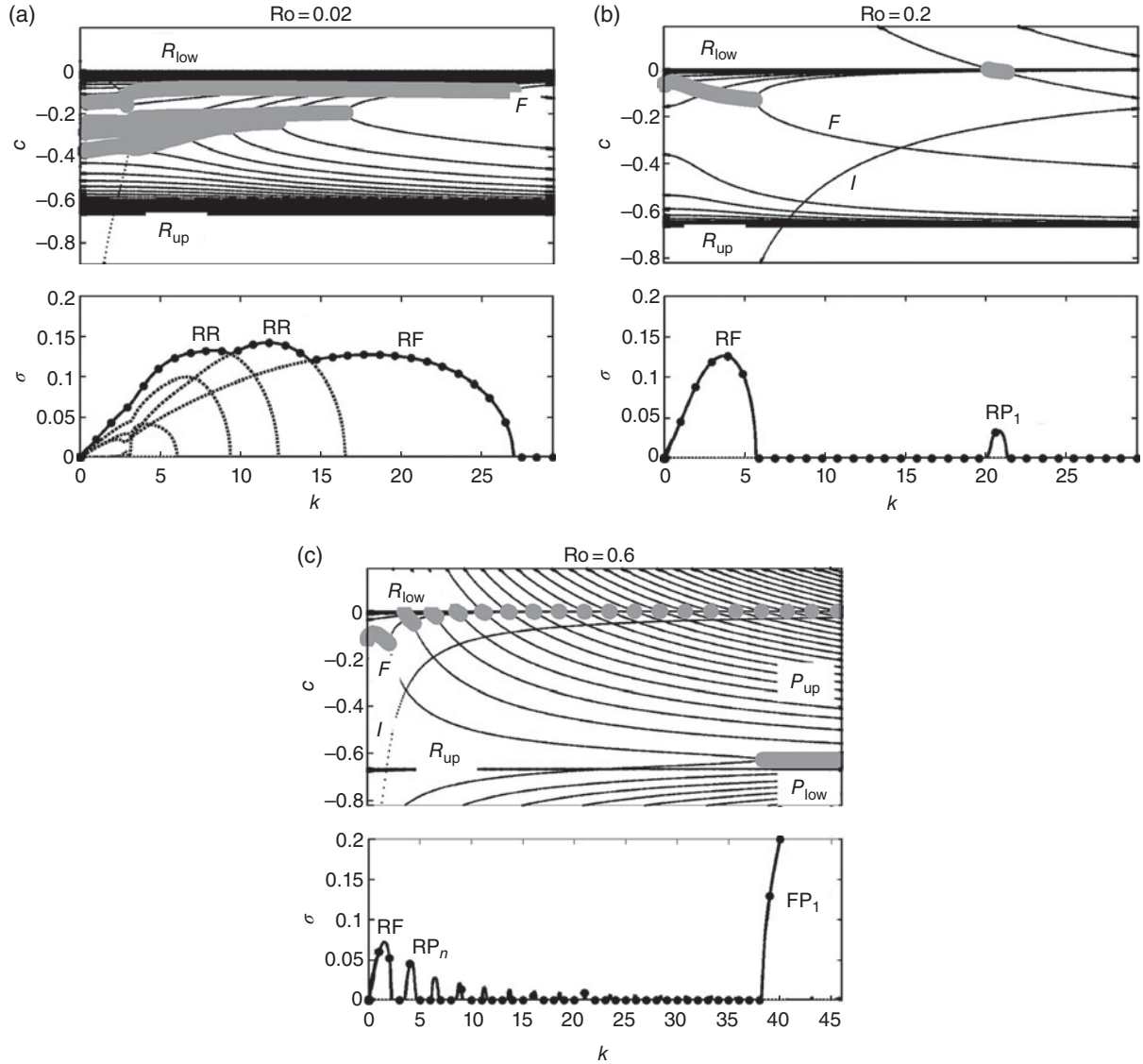


Figure 6.12. As in Figure 6.10, but with $\delta_H = 0.5$. Thick gray lines in the upper panel correspond to the unstable modes.

constant-PV layer will, in general, have low Rossby and Burger numbers and, therefore, correspond to the RF regime.

6.3.3. Comparison with Experiments

The experiments of *Griffiths and Linden* [1982] were conducted in a circular tank mounted on a rotating turntable, as in Figure 6.9, filled with a solution of density ρ_2 . The boundary current was created by injecting a lighter solution of density ρ_1 between the inner cylinder and a bottomless cylinder of radius r_c such as $r_1 < r_c < r_2$. The experiment was then initiated by

vertically withdrawing this cylinder and allowing the upper layer (height h_0 and width $L_0 = r_c - r_1$) to move under the influence of buoyancy, Coriolis, and centrifugal forces.

The upper layer is stationary before the geostrophic adjustment and therefore has constant potential vorticity. Under the assumption of no diabatic mixing taking place during the collapse, potential vorticity in the upper layer should be conserved in the final balanced state and is then written as

$$Q_1 = \frac{f + \partial_r V_1 + V_1/r}{H_1} = \frac{f}{h_0}. \quad (6.15)$$

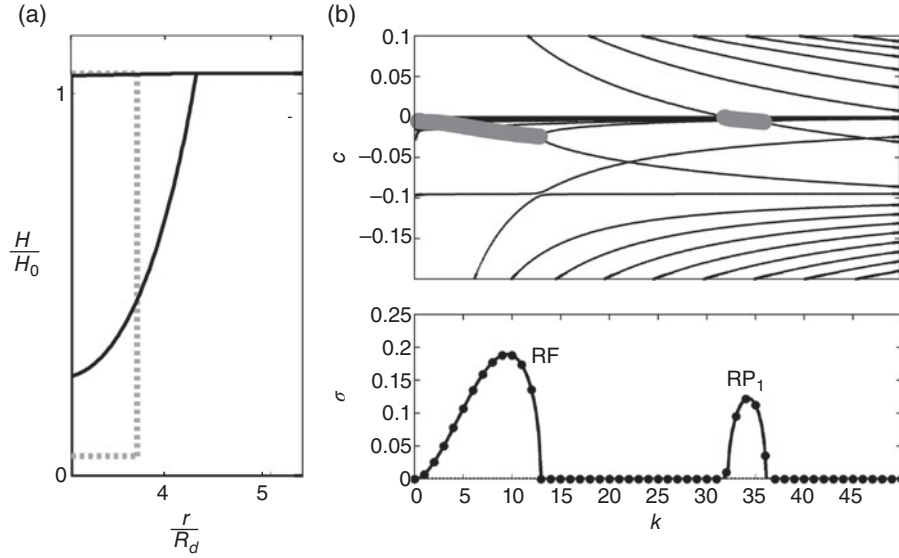


Figure 6.13. (a) Initial experimental state (dashed line) and basic state height after reaching cyclo-geostrophic equilibrium (thick line) for $F_0 = 1.4$ and $\delta_0 = 0.95$. (b) Dispersion diagram (upper panel) and growth rate (lower panel) of the eigenmodes. Thick gray lines in the upper panel correspond to the RF and RP resonances and respective unstable modes.

The steady cyclogeostrophically balanced state in each layer is given by (6.10). Assuming a bottom layer initially at rest in the rotating frame, the basic state velocity in the upper layer is then given by the solution of the following ordinary differential equation (ODE):

$$V_{1rr} + \frac{V_{1r}}{r} - \frac{V_1}{r^2} - \frac{f}{h_0 g (1 - \delta_s)} \left(f V_1 + \frac{V_1^2}{r} \right) = 0, \quad (6.16)$$

with

$$V_{1r}(r_1) = 0, \quad H_1(r_1 + L) = 0. \quad (6.17)$$

We have solved (6.16) numerically using Runge-Kutta method. The results of these calculations for two sets of parameters are shown in Figures 6.13a and 6.15a.

We use the parameters of *Griffiths and Linden* [1982], $F_0 = f^2 L_0^2 / g' h_0$, the Froude number, and $\delta_0 = h_0 / H$, the initial depth ratio. We plot for comparison two cases corresponding to (a) $F_0 = 1.4$ and $\delta_0 = 0.95$ (the dispersion diagram is shown in Figure 6.13 and the structure of the most unstable mode in Figure 6.14) and (b) $F_0 = 14.4$ and $\delta_0 = 0.19$ (the dispersion diagram is shown in Figure 6.15 and the structure of the most unstable mode in figure 6.16). Photographs of the corresponding laboratory experiments (Figures 3 and 4, respectively in [*Griffiths and Linden*, 1982]) are reproduced in Figures 6.14d and 6.16d,

and one can see a perfect agreement with the observed wave numbers for these experiments.

In both cases the most unstable wave number corresponds to the RF mode. The Rossby eigenmodes are absent in the upper layer owing to the uniformity of PV. As seen from the comparison with equation (6.10), the corresponding set of dispersion curves $c \approx -U_0$ is absent in Figures 6.13 and 6.15. However, as was already discussed in the previous section, the frontal mode has the characteristics of a Rossby wave for low wave numbers, and the RF mode is therefore very similar to the classical baroclinic instability.

Photographs of the laboratory experiments (Figure 6.14d and 6.16d) show the instability at a later nonlinear stage as compared to the initial linearly growing stage computed by linear analysis. The nonlinear evolution of the RF instability in the rectilinear two-layer shallow-water model was simulated by *Gula et al.* [2010]. The frontal disturbances were observed to evolve in agreement, modulo rectilinear geometry, with the sequence of photographs of *Griffiths and Linden* [1982], and ultimately led to the formation and detachment of outward propagating cyclone-anticyclone vortex pairs, as observed in the work of *Griffiths and Linden* [1982] and *Thivolle-Cazat and Sommeria* [2004].

The stability analysis has been repeated for different values of the inner cylinder radius r_1 (not shown) and reproduces the results of *Griffiths and Linden* [1982], demonstrating a small influence of this parameter and hence of the wall in such a configuration. It is interesting to note that the RF instability was interpreted, even for

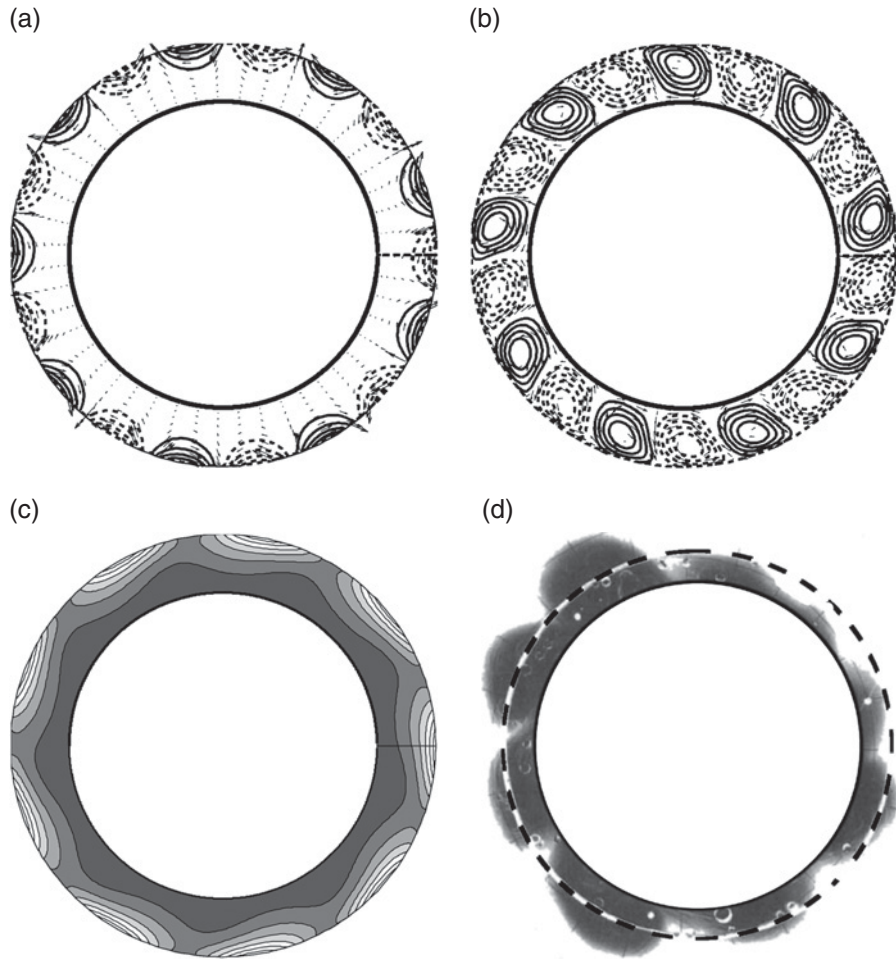


Figure 6.14. Pressure and velocity fields of (a) upper and lower (b) layers and (c) interface height of the baroclinically unstable mode at $k = 9$ ($kR_d = 14.5$, see Figure 6.13). Full lines: positive; dotted lines: negative values. The field in the upper layer is typical for a frontal mode, while the field in the lower layer is typical for a Rossby mode. (d) Photograph of the corresponding experiment adapted from *Griffiths and Linden [1982]*.

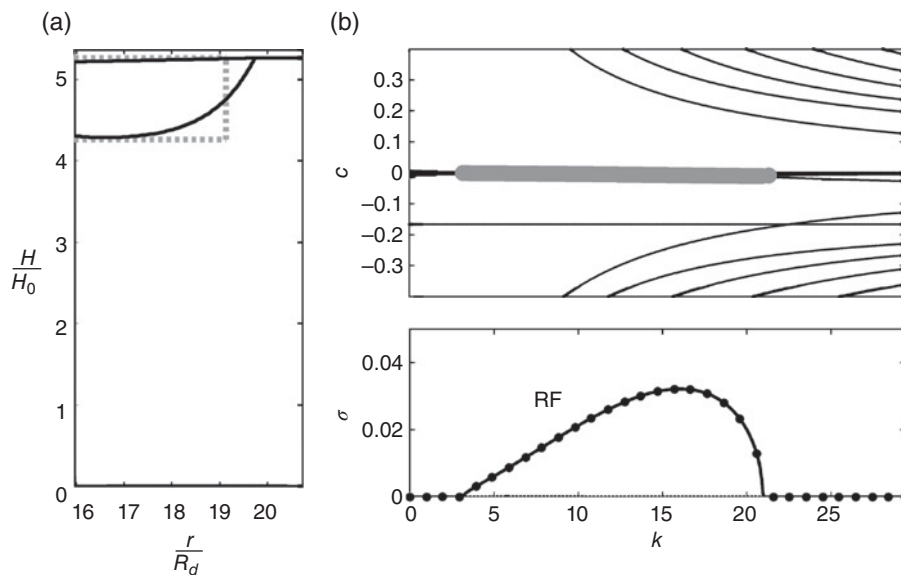


Figure 6.15. (a) Initial experimental state (dashed line) and basic state height after reaching cyclo-geostrophic equilibrium (thick line) for $F_0 = 14.4$ and $\delta_0 = 0.19$. (b) Dispersion diagram (upper panel) and growth rate (lower panel) of the eigenmodes. Thick gray lines in the upper panel correspond to the RF and RP resonances and respective unstable modes.

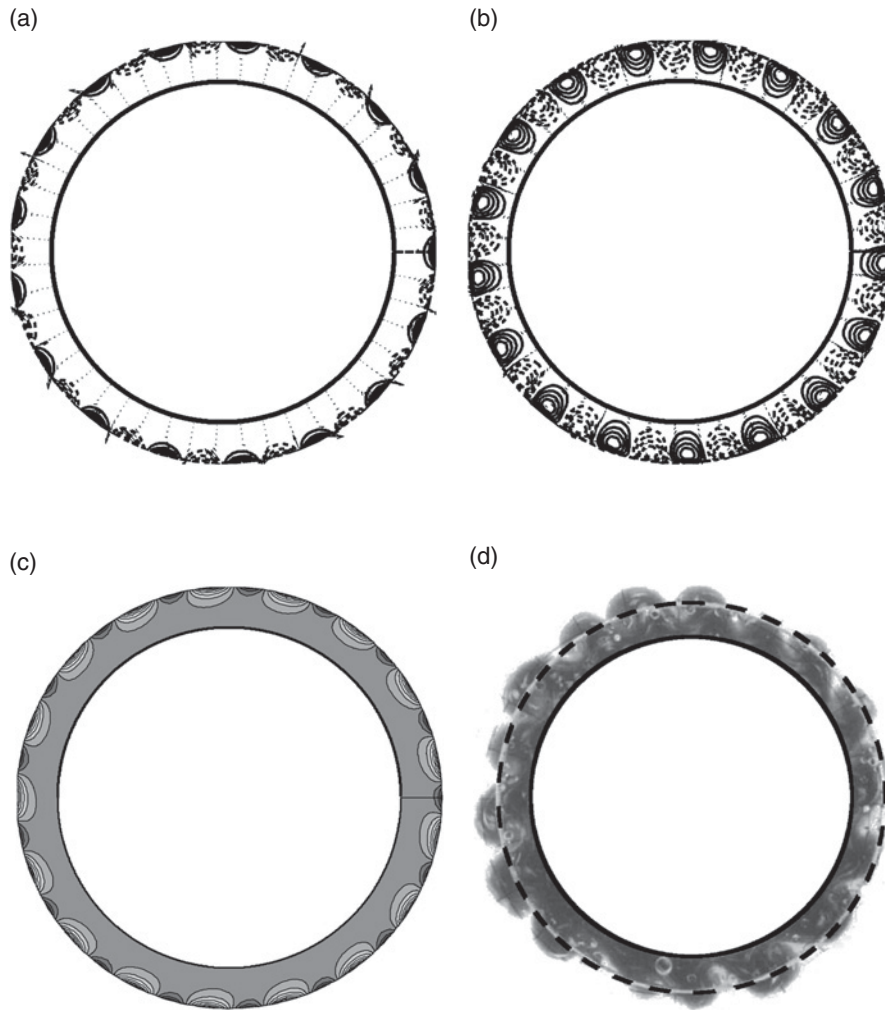


Figure 6.16. Pressure and velocity fields of the upper (a) and lower (b) layers and (c) interface height of the baroclinically unstable mode at $k = 17$ ($kR_d = 5$, see Figure 6.15). Full lines: positive; dotted lines: negative values. The field in the upper layer is typical for a frontal mode, while the field in the lower layer is typical for a Rossby mode. (d) Photograph of the corresponding experiment adapted from *Griffiths and Linden* [1982].

small Rossby numbers, as ageostrophic by many authors, because the uniform PV in the upper layer does not satisfy the Charney-Stern theorem of the PV gradient inversion between the two layers. Yet, it is still possible to interpret it as generalized quasi-geostrophic instability; see a discussion of this point by *Boss et al.* [1996].

6.4. IMPACT OF BATHYMETRY ON INSTABILITIES

In this section we study the impact of bathymetry in a form of a constant-slope shelf on the stability of the flow. We use the same set of equations and parameters as in the previous section with the addition of a bottom topography with height $H_t(r)$. Following *Pennel et al.* [2012], we

define a topography parameter To as the ratio of the shelf slope γ to the isopycnal slope α ,

$$To = \frac{\gamma}{\alpha}, \quad (6.18)$$

where α is defined as the slope of the interface between the layers at the location of the front. The parameter To has been found relevant for quantifying the shelf impact on the surface current (*Pennel et al.* [2012]), as was previously suggested by works in the quasi-geostrophic Phillips model. Positive values of To , as in Figure 6.9, correspond to isopycnal and shelf slopes in the same direction, which is typical of upwelling events along the coast of western boundary currents. Negative values of To correspond to

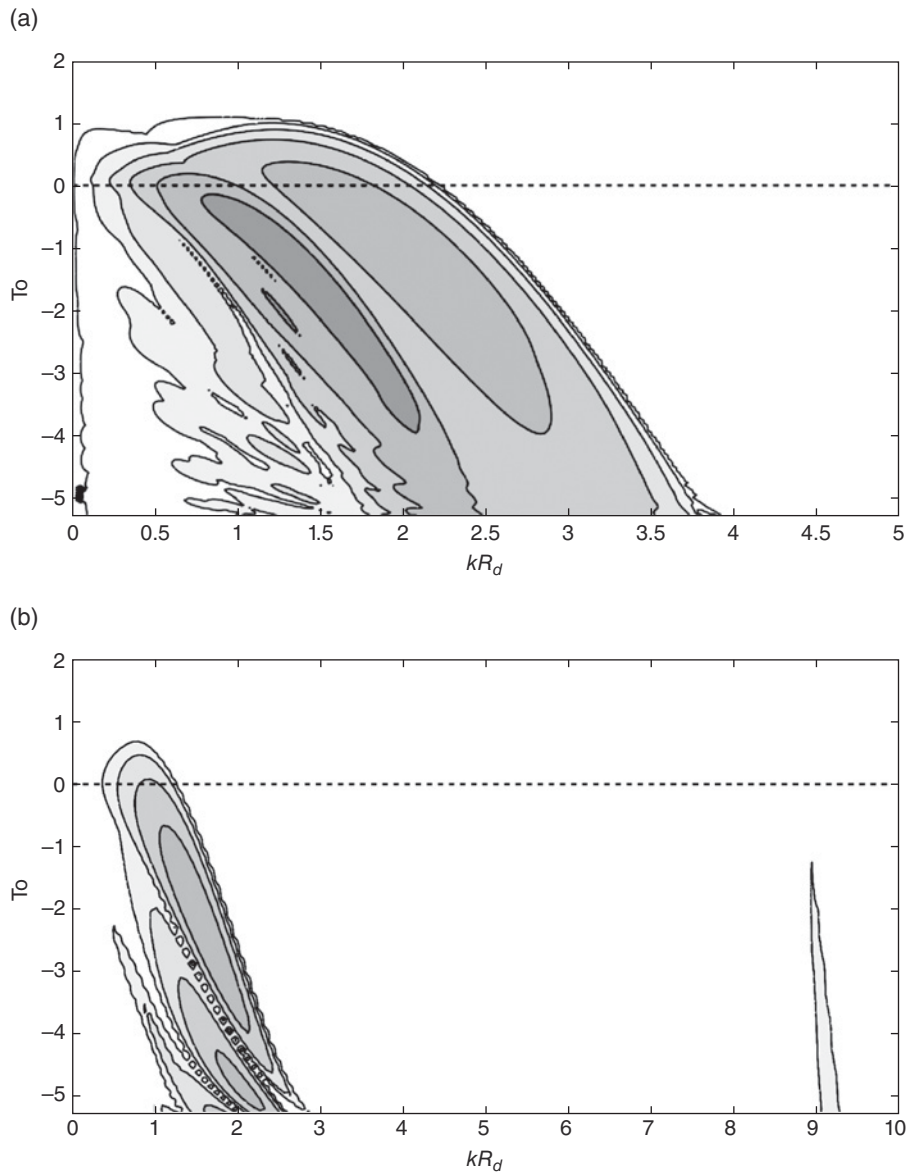


Figure 6.17. Growth rate of the most unstable modes as a function of the topography parameter To for (a) $Ro = 0.02$ and (b) $Ro = 0.2$ with $\delta_H = 0.1$

isopycnal and shelf slopes in the opposite directions and are typical of buoyant coastal currents.

In order to study the influence of the topography on the stability of the current and to vary the parameter To without changing other parameters, we will define the aspect ratio between the two layers as $\delta H = H_1(r_1)/H_2(r_1 + L)$ and keep it constant while varying the topography height.

The novelty of the configuration with nontrivial topography is that the latter allows for specific topographic waves, in addition to frontal, Kelvin, Rossby, and Poincaré waves discussed above. These waves may resonate with

other types of waves and thus lead to new instabilities. On the other hand, topography changes the propagation speed of these waves and may thus “detune” the resonances, leading to stabilization of the flow. We observe both effects, depending on To .

Figure 6.17 shows the growth rates of the most unstable modes as a function of To and nondimensional wave number for the set of parameters used in the dispersion diagrams of Figures 6.10a, 6.10b, and 6.12c. In all cases there is a strong stabilization of the flow for a positive To , with growth rates vanishing for To close to 1

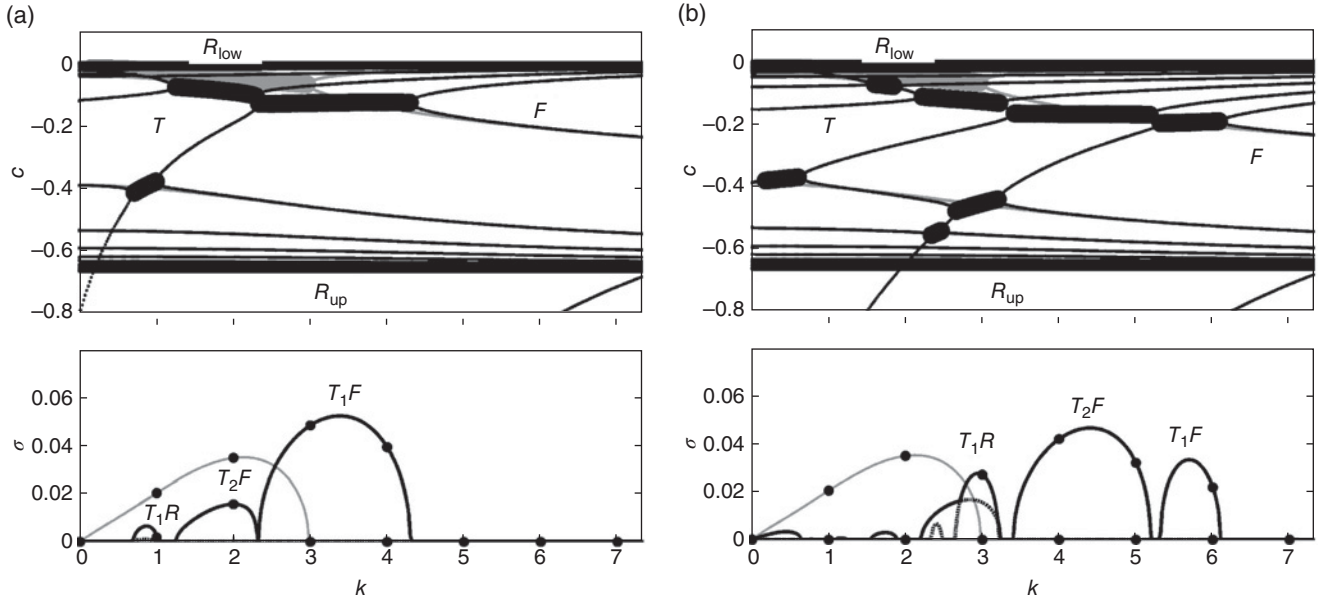


Figure 6.18. Dispersion diagram (upper panel) and growth rate (lower panel) of the eigenmodes for: (a) $Ro = 0.2$ and $To = -2$ and (b) $To = -5$. Thick black lines in the upper panel correspond to the TF and TR resonances and respective unstable modes. Gray lines in both panels correspond to the same case with no topography (Figure 6.10b).

(topography almost parallel to the interface). It is clear from the expressions for the PV gradient in the lower layer,

$$\partial_r Q_2 = -f \frac{\partial_r H_2}{H_2^2}, \quad (6.19)$$

and for the topography parameter,

$$To = \frac{\partial_r H_t}{\partial_r H_2 + \partial_r H_t} \Big|_{r_1+L}, \quad (6.20)$$

that $To \rightarrow 1$ will imply $\partial_r Q_2 \rightarrow 0$, which explains the stabilization.

In Figure 6.18 we present the stability diagrams at two different negative values of To at $Ro = 0.2$ showing that the most unstable modes in such configurations are due to the resonances of a frontal wave with a topographic wave (either the first T_1 or the second T_2 radial mode), although the resonances of the first topographic mode with a Rossby wave are also observed. Figure 6.19 displays the corresponding unstable modes. Thus, topography plays a crucial role in the destabilization of the flow in this regime.

6.5. SUMMARY AND DISCUSSION

We thus performed a stability analysis of the shear flows in the rotating annulus in the framework of the two-layer shallow-water model in the wide range of

parameters, both in the superrotating rigid-lid and free-surface outcropping configurations, including topography effects in the latter case. We got a detailed structure of the unstable modes to be compared with the experimental results in these configurations. Such a comparison shows a good agreement with the density-current experiments. The experiments with two-layer fluid with superrotating lid do show the RK instability as follows from the analysis of *Flór et al.* [2011], with good quantitative agreement with two-layer shallow-water results, while short-wave structures on the background of Rossby waves, which were observed in experiments of *Williams et al.* [2005] and *Flór* [2007]), do not find a direct explanation in terms of dominant unstable modes that we found. This means that these short-wave structures are probably due to the fine vertical structure of the interface between the layers, which does not exist in the shallow-water approximation (see a discussion by *Flór et al.* [2011] on this subject as well as Chapter 11 in this volume). Our results on the influence of topography on the instabilities show that in the case of opposite orientations of the isopycnal and shelf slopes the destabilization of density currents is due to resonances of Rossby and topographic waves, and thus the influence of topography may be crucial.

Acknowledgments. The work of V. Zeitlin was supported by the French ANR grant SVEMO.

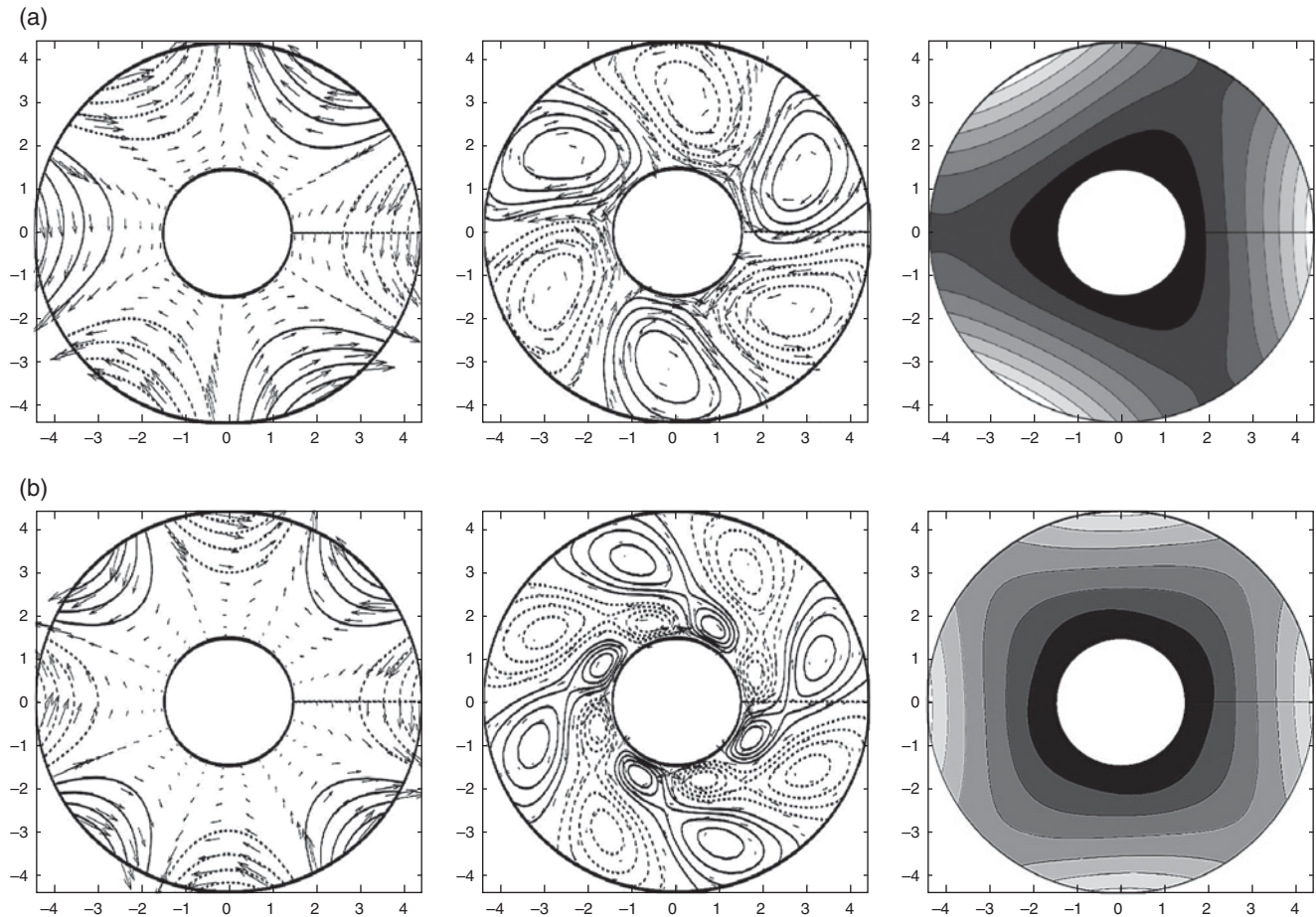


Figure 6.19. Pressure and velocity fields of the upper (left) and lower (middle) layers and interface height (right) of the most unstable mode for $Ro = 0.2$ and (a) $To = -2$ (see Figure 6.18a) and (b) $To = -5$ (see Figure 6.18b). Full lines: positive; dotted lines: negative values.

REFERENCES

- Boss, E., N. Paldor, and L. Thompson (1996), Stability of a potential vorticity front: From quasi-geostrophy to shallow water, *J. Fluid Mech.*, *315*, 65–84.
- Cairns, R. A. (1979), The role of negative energy waves in some instabilities of parallel flows, *J. Fluid Mech.*, *92*, 1–14.
- Dunkerton, T., P. Lelong, and C. Snyder (Eds.) (2008), Spontaneous imbalance, *J. Atmos. Sci.*, special collection.
- Flór, J.-B. (2007), Frontal instability, inertia-gravity wave radiation and vortex formation, in *Proceedings of the 18th CFM Conference, Grenoble, France*.
- Flór, J.-B., H. Scolan, and J. Gula (2011), Frontal instabilities and waves in a differentially rotating fluid, *J. Fluid Mech.*, *685*, 532–542.
- Ford, R. (1994), Gravity wave radiation from vortex trains in rotating shallow water, *J. Fluid Mech.*, *281*, 81–118.
- Fultz, D., R. R. Long, G. V. Owens, W. Bohan, R. Kaylor, and I. Weil (1959), Studies of thermal convection in a rotating cylinder with some implications for large-scale atmospheric motions, *Met. Monogr.*, *4*, 1–104.
- Griffiths, R. W., and P. F. Linden (1982), Part I: Density-driven boundary currents. *Geophys. Astrophys. Fluid Dyn.*, *19*, 159–187.
- Griffiths, R. W., P. D. Killworth, and M. E. Stern, (1982), Ageostrophic instability of ocean currents, *J. Fluid Mech.*, *117*, 343–377.
- Gula, J., and V. Zeitlin (2010), Instabilities of buoyancy driven coastal currents and their nonlinear evolution in the two-layer rotating shallow water model. Part I. Passive lower layer, *J. Fluid Mech.*, *659*, 69–93.
- Gula, J., R. Plougonven, and V. Zeitlin, (2009a), Ageostrophic instabilities of fronts in a channel in the stratified rotating fluid, *J. Fluid Mech.*, *627*, 485–507.
- Gula, J., V. Zeitlin, and R. Plougonven (2009b), Instabilities of two-layer shallow-water flows with vertical shear in the rotating annulus, *J. Fluid Mech.*, *638*, 27–47.
- Gula, J., V. Zeitlin, and F. Bouchut (2010), Instabilities of buoyancy driven coastal currents and their nonlinear evolution in the two-layer rotating shallow water model. Part II. Active lower layer, *J. Fluid Mech.*, *665*, 209–237.
- Hart, J. E. (1972), A laboratory study of baroclinic instability, *Geophys. Astrophys. Fluid Dyn.*, *3*, 181–209.

- Hayashi, Y.-Y. and W. R. Young (1987), Stable and unstable shear modes of rotating parallel flows in shallow water, *J. Fluid Mech.*, 184, 477–504.
- Hide, R. (1958), An experimental study of thermal convection in a rotating liquid, *Phil. Trans. R. Soc. London Ser. A Math. Phys. Sci.* 250(983), 441–478.
- Hide, R. and W. W. Fowlis (1965), Thermal convection in a rotating annulus of liquid: Effect of viscosity on the transition between axisymmetric and non-axisymmetric flow regimes, *J. Atmos. Sci.* 22, 541–558.
- Hoskins, B. J., M. E. McIntyre, and A. W. Robertson (1985), On the use and significance of isentropic potential vorticity maps, *Q. J. R. Meteorol. Soc.*, 111(470), 877–946.
- Iga, K. (1993), Reconsideration of Orlandi's instability theory of frontal waves, *J. Fluid Mech.*, 255, 213–236.
- Lovegrove, A. F., P. L. Read, and C. J. Richards, (2000), Generation of inertia-gravity waves in a baroclinically unstable fluid, *Q. J. R. Meteorol. Soc.*, 126, 3233–3254.
- Meacham, S. P., and J. C. Stephens (2001), Instabilities of gravity currents along a slope, *J. Phys. Oceanogr.*, 31, 30–53.
- O'Sullivan, D., and T. J. Dunkerton (1995), Generation of inertia-gravity waves in a simulated life cycle of baroclinic instability, *J. Atmos. Sci.*, 52(21), 3695–3716.
- Paldor, N., and M. Ghil, (1991), Shortwave instabilities of coastal currents, *Geophys. Astrophys. Fluid Dyn.*, 58, 225–241.
- Pennel, R., A. Stegner, and K. Beranger (2012), Shelf impact on buoyant coastal current instabilities, *J. Phys. Oceanogr.*, 42, 39–61.
- Reznik, G. M., V. Zeitlin, and M. Ben Jelloul (2001), Nonlinear theory of geostrophic adjustment. Part 1. Rotating shallow-water model, *J. Fluid Mech.*, 445, 93–120.
- Ripa, P. (1983), General stability conditions for zonal flows in a one-layer model on the β -plane or the sphere, *J. Fluid Mech.*, 126, 463–489.
- Sakai, S. (1989), Rossby-Kelvin instability: A new type of ageostrophic instability caused by a resonance between Rossby waves and gravity waves, *J. Fluid Mech.*, 202, 149–176.
- Thivolle-Cazat, E., and J. Sommeria (2004), in *Shallow Flows*, edited by G. H. Jirka and W. S. J. Uijttewaal, pp. 23–30, An experimental investigation of a boundary current instability, Taylor and Francis Group, London.
- Trefethen, L. N. (2000), *Spectral Methods in Matlab.*, SIAM, Philadelphia, Penna.
- Williams, P. D., P. L. Read, and T. W. N. Haine (2004), A calibrated, non-invasive method for measuring the internal interface height field at high resolution in the rotating, two-layer annulus, *Geophys. Astrophys. Fluid Dyn.*, 98, 453–471.
- Williams, P. D., T. W. N. Haine, and P. L. Read (2005), On the generation mechanisms of short-scale unbalanced modes in rotating two-layer flows with vertical shear, *J. Fluid Mech.*, 528, 1–22.
- Zeitlin, V. (2008), Decoupling of balanced and unbalanced motions and inertia-gravity wave emission: Small versus large Rossby numbers, *J. Atmos. Sci.*, 65, 3528–3542.